Materials Transactions, Vol. 65, No. 5 (2024) pp. 587 to 596

A Comparative Investigation of Corrosion Behavior and the Concurrent Acoustic Emission of AZ31 Mg Alloy under NaCl and Na_2SO_4 Solution Droplets

Kaige Wu[1,*], Kaita Ito[2] and Manabu Enoki[1]

[1]*Department of Materials Engineering, The University of Tokyo, Tokyo 113-8656, Japan*
[2]*Materials Modeling Group, Center for Basic Research on Materials, National Institute for Materials Science, Tsukuba 305-0044, Japan*

In this work, corrosion behavior and the concurrent acoustic emission (AE) signals of AZ31 alloy under NaCl and Na_2SO_4 solution droplets were comparatively investigated in combination with *in-situ* optical microscopy observations. It was observed that after a short initial corrosion accompanied by the growth and rupture of H_2 bubbles, the later corrosion behavior of AZ31 alloy mainly developed into filiform corrosion under NaCl solution droplet and pitting corrosion under Na_2SO_4 solution droplet. AE signals were detected in both cases. In particular, AE parameters of amplitude and duration were found to well identify filiform and pitting corrosion. AE signals were mainly correlated with the observed evolution of H_2 bubbles of different shapes and positions, i.e., regularly round bubbles grew and ruptured at the filament head near the metal surface during filiform corrosion; whereas irregularly-shaped bubbles grew and ruptured at the pit mouth during pitting corrosion.
[doi:10.2320/matertrans.MT-M2023190]

(Received November 28, 2023; Accepted February 13, 2024; Published February 26, 2024)

Keywords: *magnesium, atmospheric corrosion, filiform corrosion, pitting corrosion, hydrogen bubble evolution, acoustic emission*

1. Introduction

It is worth noting that, as the lightest material among all engineering metals, magnesium (Mg) alloys are fast replacing denser materials in terms of lightweight components, not only iron-based and copper-based but even aluminum-based alloys, in many industrial applications.[1)] However, they can suffer from corrosion in the marine atmosphere.[2,3)] Particularly, the increasing use of Mg-Al-Zn (AZ) series alloys, the best known as AZ31, in the automotive industry and marine engineering,[1,4)] makes their atmospheric corrosion a timely matter of concern.

Many endeavors adopting the strategies of field-exposed test[5–8)] or laboratory simulation test[9–14)] have been carried out in the last few decades in understanding the atmospheric corrosion behavior. Concerning the corrosion form, localized corrosion was the most widely referred form accounting for the atmospheric corrosion of AZ alloys.[5,8–12)] From a 24-month-long study of field-exposed AZ31 alloy in the tropical marine atmosphere, Cui *et al.*[8)] found that the corrosion evolution experienced a turning point, which was corresponding to the sixth month, from the initial pitting corrosion to the subsequent general corrosion. Another series of studies in simulating the atmospheric corrosion in laboratory, typically reported by Merino *et al.*[9)] and Arrabal *et al.*[10)] who exposed AZ31 and AZ91 alloys in NaCl spray frog, Arrabal *et al.*[11)] who exposed AZ31 alloy in high humidity atmospheres, Jonsson *et al.*[12)] who exposed the AZ91D alloy under a NaCl solution droplet in the humid air, consistently reported the corrosion developing as pitting corrosion. Besides, another critical corrosion form is filiform corrosion, which has been frequently reported on the uncoated AZ91[15,16,20)] and AZ31 alloys[17–19)] in the full immersion corrosion tests as dark, shallow thread-like tracks driven by anodic Mg dissolution at the filament head and the galvanically coupled hydrogen evolution in the cathodically activated region behind. However, very limited reports were found for filiform corrosion during atmospheric corrosion of Mg alloys. Moreover, comparing with the relatively many studies of chloride-induced atmospheric corrosion,[8–10,12,20)] investigation on the atmospheric corrosion behavior of AZ alloys in the environment containing sulfate (SO_4^{2-}) ion, one of the dominant anions in the rainwater and seawater,[3,21)] has been very limited. Therefore, comparatively investigating the chloride- and sulfate-induced atmospheric corrosion behavior of AZ alloy is the primary concern of present work.

On the other hand, atmospheric corrosion of Mg alloys is inherently a typical electrochemical phenomenon occurring under a thin electrolyte layer, which is deeply influenced by multiple factors and therefore difficult to predict based on prior-data.[2,4)] From this aspect, monitoring atmospheric corrosion of Mg alloys especially at its early stage has become more realistic to prevent corrosion-induced failure and accidents. Acoustic emission (AE) is a typical *in-situ* nondestructive evaluation (NDE) method which detects transient elastic waves generated by rapid energy release from localized sources within the material.[22)] AE method has long been used to study the metal corrosion. However, most attentions including the latest AE reports,[23–33)] have been paid on the steel corrosion. The literature[34–39)] on AE studies on the corrosion of Mg and Mg alloys is very limited. The earliest AE research of Mg alloys in literature can be traced back to the work in 1975[34)] by Chakrapani and Pugh who detected discrete AE signals from discontinuous crack advance during the propagation of transgranular stress-crrosion cracking of a Mg-7.5%Al alloy in an aqueous NaCl-K_2CrO_4 solution. After that, the AE method was used to study the corrosion fatigue of AZ31 alloy[35)] and AE energy release was found to be associated with the corrosion fatigue damage. Recently, several trials combined AE method and electrochemical measurements to study pitting corrosion of pure Mg,[36,37)] WE43 alloy,[37)] and AZ31 alloy.[38,39)] From the main conclusions,[36,37,39)] the rupture of passive film during pit initiation and hydrogen (H_2) bubble evolution

*Corresponding author, E-mail: kaigewu@rme.mm.t.u-tokyo.ac.jp

during pit propagation could be monitored by detecting the corresponding AE signals. Besides, ion exchange and film-forming process were also proposed to be the possible AE source mechanisms through advanced clustering analysis of AE data[37] or comparison with the electrochemical noise (EN) signals.[39] In general, these works show the feasibility of AE method in probing the localized corrosion of Mg alloys.[36–39] However, these AE studies so far were assigned on the electrochemically controlled pitting corrosion of Mg alloys. To the best of authors' knowledge, there are no reports yet on the AE investigation of atmospheric corrosion of Mg alloys, which is another concern of this study.

In this work for the first time, real-time AE monitoring combined with *in-situ* optical microscopic observation was proposed to study the atmospheric corrosion behavior of AZ31 alloy under a droplet of two salt solutions (i.e., NaCl solution and Na_2SO_4 solution, respectively) in a high humidity atmosphere. Different corrosion behavior in terms of different AE responses were comparatively studied.

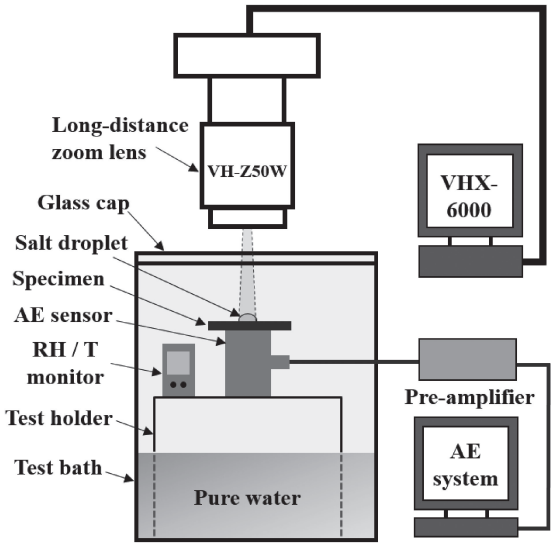

Fig. 1 Schematic of the experimental setup, including droplet corrosion testing in a high humidity bath, AE measurements, and real-time *in-situ* observations via long-distance zoom lens (VH-ZW50W) with high-resolution image digital microscope (VHX-6000).

2. Experimental

2.1 Material and microstructure

A rolled AZ31 Mg alloy sheet (Al: 3.2, Zn: 1.08, Mn: 0.42, Si: 0.0024, Fe: 0.0022, Cu: 0.002, Ni: 0.0007, Mg: balance, mass%) was used for this study. Corrosion specimens of 10.0 mm × 10.0 mm × 2.0 mm were cut in the RD–TD plane. The specimen surface was polished until using 1.0 μm alumina slurry, subsequently cleaned with ethanol and dried with a jet of compressed air. The phase composition was analyzed with X-ray diffraction (XRD) measurement using a 9-kW diffractometer (Cu Kα radiation source; Rigaku SmartLab, Japan). The grain size of AZ31 alloy was observed after chemical etching using a solution of ethanol (100 ml), picric acid (5 g), acetic acid (5 ml) and water (10 ml).

2.2 Droplet corrosion tests and AE measurements

Figure 1 shows the experimental setup. Corrosion tests were performed in a test bath of constant 99% relative humidity (RH) and 24.9 ± 0.1°C. Corrosion specimens were comparatively exposed to a single droplet of 1.0 μL 0.1 mass% NaCl solution or Na_2SO_4 solution to compare the corrosion behavior. Simultaneously, the AE measurement was performed using a custom AE acquisition system of continuous wave memory (CWM) developed in our group.[40] A high-sensitivity R-CAST sensor system including AE transducer of the resonant frequency 200 kHz (M204A, Fuji Ceramics Corp., Japan) was employed to record the AE streaming data at the sampling rate of 5 MHz. The combined use of AE sensor with internal head-amplifier and pre-amplifiers (A1002, Fuji Ceramics Corp. Japan) enabled the sensor system to achieve a gain of 55 dB for AE detection. After AE measurements, a threshold of 20 mV (comparable to 30.8 dB), which was confirmed to be higher than the background noise level, was used to isolate AE signal events from the continuously recorded waveforms. Simultaneously, AE parameters[41] of each signal event were calculated by CWM. During the whole testing, the specimen surface under the droplet was monitored via a long-distance lens (VH-ZW50W) and an optical microscope (VHX-6000, Keyence Corp., Osaka, Japan) with a recording interval of 15 seconds.

2.3 Analysis of corrosion products and corrosion morphologies

After corrosion testing, corrosion specimens were immediately inspected by XRD measurements to analyze the corrosion products. Corrosion morphologies were examined using a lab-based X-ray computed tomography (XCT) system (ZEISS Xradia 520 Versa, Carl Zeiss XRM, Pleasanton, CA, USA). A fine resolution of 0.8 μm/voxel was optimized to reveal the interior morphology of the corrosion region. The surface morphology of the corrosion was observed by scanning electron microscope (SEM, JCM-6000, NeoScope, JEOL, Japan). Moreover, a SEM equipped with focused ion beam (FIB) system with an EDS unit (JIB-4700F Multi Beam System, JEOL, Japan) was used to analyze the cross-sectional morphologies of corrosion sites.

3. Results

3.1 Initial microstructure

Figure 2(a) shows the XRD pattern of AZ31 alloy indicating the main phase consisting of α-Mg and Al-Mn intermetallic inclusions with two stoichiometries of Al_6Mn and Al_8Mn_5, which is consistent with previous reports[5,9,11]

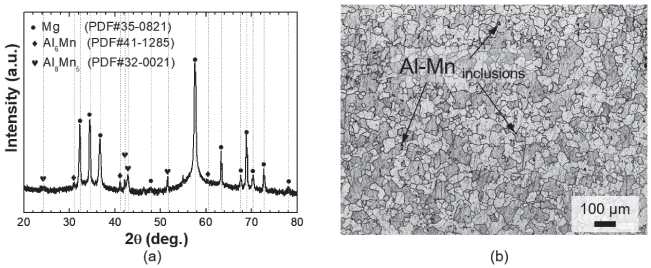

Fig. 2 (a) Microstructure and (b) XRD pattern of AZ31 alloy investigated.

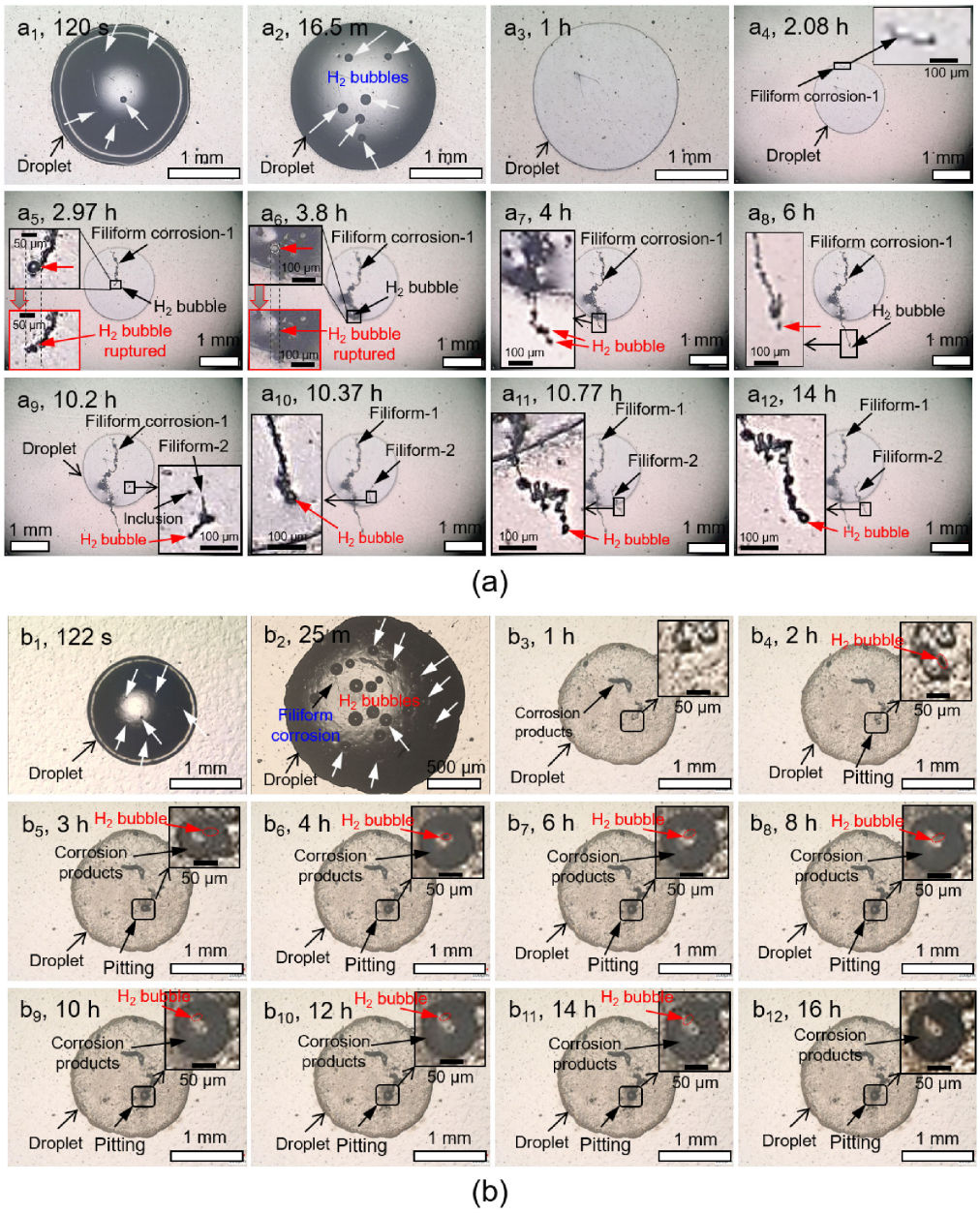

Fig. 3 *In-situ* observation of the corrosion behavior of AZ31 alloy under the droplets of NaCl (a) and Na_2SO_4 (b) solution, respectively.

on the microstructure of AZ31 alloy. Figure 2(b) shows the microstructure with few AlMn inclusions that were randomly presented in the interior of grains and grain boundaries. The mean grain size was determined to be $d = 34.8$ μm based on the line intercept method.

3.2 Corrosion behavior and AE evolution

Figure 3 and 4 shows the corrosion behavior and AE evolution of AZ31 alloy under NaCl and Na_2SO_4 solution droplet, respectively. The corrosion tests under NaCl and Na_2SO_4 solution droplets were held for 14.58 h (52,488 seconds) and 17.625 h (63,450 seconds), producing 147 and 237 AE events, respectively. In general, it was observed that the filiform corrosion predominantly occurred from the NaCl solution droplet, while the pitting corrosion mainly developed under the Na_2SO_4 solution droplet.

Figure 3(a) and 4(a) shows the case under NaCl solution droplet. According to the corrosion evolution over time, the AE signal in Fig. 4(a) was divided into two regions, i.e., the initial corrosion as presented in Fig. 3(a_1)–(a_3) and the subsequent filiform corrosion as presented in Fig. 3(a_4)–(a_{12}). After a short time since the specimen was exposed to the droplet (Fig. 3(a_1)), H_2 bubbles began to form. The H_2 bubbles of increasing number seemed to be randomly distributed on the specimen surface under the droplet (Fig. 3(a_2)). As the corrosion proceeded and the droplet layer thinned, H_2 bubbles ruptured one by one. During this process, the AE signals were detected along with the H_2 bubble evolution. In particular, it was found that the growth and rupture of H_2 bubbles were clearly reflected by two AE groups, as marked in Fig. 4(a), and the bubble rupture process produced more strong AE signals. After about 1 h, all bubbles ruptured and the specimen surface became temporarily "quiet" both in the surface change and AE detection. Subsequently, filiform corrosion began to be initiated after 2 h (Fig. 3(a_4)). It was observed that two single-tracks of filiform

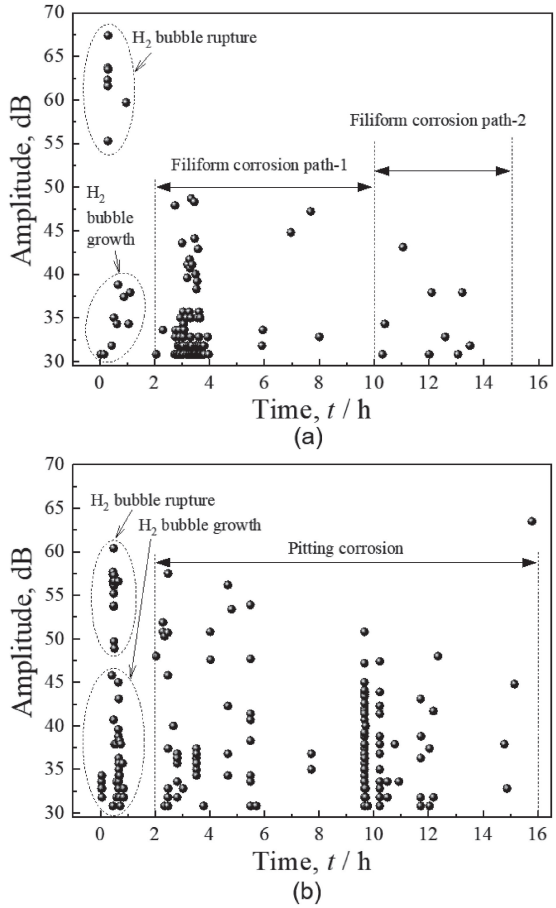

Fig. 4 Evolution of AE signals during the corrosion of AZ31 alloy under the droplets of NaCl (a) and Na_2SO_4 (b) solution.

corrosion developed successively from the NaCl droplet. During the filiform corrosion propagation, localized corrosion occurred along the filament path with the H_2 bubble evolution, as highlighted in Fig. 3(a_5), (a_6), (a_7), and (a_{10}). The most noticeable feature captured for filiform corrosion propagation is the evolution of H_2 bubble at the filament head, i.e., one H_2 bubble always developed at the filament head before the filament path propagated forward, as observed in Fig. 3(a_5)–(a_{12}). It was highlighted in Fig. 3(a_5) that when the H_2 bubble ruptured, the filament path propagated one step forward, suggesting that the H_2 bubble evolution is an important phenomenon in relation to the propagation of filiform corrosion. On the other hand, AE signals were mostly detected between 2 and 4 h. It was found that the initiation and propagation of filament path did not produce detectable AE signals; but the detection of AE signals was well corresponding to the rupture event of H_2 bubbles locating at the filament head.

Figure 3(b) and 4(b) shows the case under Na_2SO_4 solution droplet. Similarly, the AE signal was divided into two stages according to the corrosion evolution over time, i.e., the initial corrosion as presented in Fig. 3(b_1)–(b_3) and the later pitting corrosion as presented in Fig. 3(b_4)–(b_{12}). Initially, the Na_2SO_4 droplet caused the localized corrosion which was indicated by the occurrence of single, randomly-distributed H_2 bubbles, as presented in Fig. 3(b_1). Specifically, some short filiform-like corrosion also occurred but shortly ceased (Fig. 3(b_2)). Finally, all H_2 bubbles ruptured and the exposed region under droplet became temporarily "quiet" both in the surface change and AE detection after about 1 h (Fig. 3(b_3)). It is interesting that the rupture events of H_2 bubbles were corresponding to one AE group and the growth of H_2 bubbles was observed to be another AE group, as marked in Fig. 4(b).

Subsequently, as presented in Fig. 3(b_4), the pitting corrosion was observed to be initiated with the H_2 bubble evolution. As the corrosion developed, corrosion products in black color precipitated with a circular morphology (Fig. 3(b_5)–(b_7)). The center area in light color is believed to be the mouth of pitting corrosion. The H_2 bubble was observed to rupture at the very site of the pit mouth (Fig. 4(b_6)–(b_{11})). During the pitting corrosion, AE signals were detected together with the rupture event of H_2 bubbles. This result is consistent with the mostly-reported localized corrosion in steels,[24,26–29,32,33] pure Mg, and Mg alloys.[37] It should be noted that the H_2 bubble evolution was not continuously observed during the corrosion process, which was also reflected in the AE response, i.e., no bubble evolution or almost no AE signals were recorded during about 5.9–9.4 h and 12.5–14.4 h. Besides, the captured H_2 bubbles were irregular in shape, which is largely different from the bubbles of regularly-round shape during filiform corrosion of AZ31 alloy exposed to NaCl solution droplet.

3.3 AE waveforms and parameters

Figure 5 shows the typical AE waveforms of H_2 bubble growth during the initial corrosion. The signals are generally similar in the comparable amplitude level and similar waveform shape. The growth of H_2 bubble during metal corrosion has long been regarded as one of the typical source of AE signals during H_2 bubble evolution.[25–27,30,33,38] According to a recent microelectrochemical study with high-speed microscope during pit initiation in aluminum alloy,[42] which successfully separated and captured the growth of a single H_2 bubble, it was revealed that peak frequency of the concurrent AE signals decreased as the bubble grew up. The dependence of AE frequency on the bubble size was found to fit well with Minnaert's model,[43] which quantitatively explained the acoustic mechanism in terms of volumetric oscillations at the wall of a growing gas bubble in liquid. In this work, the growth of bubbles at the early stage of droplet corrosion, which was monitored with AE signals, was reasonably proposed as one of the AE sources. Figure 6 shows the waveform of the H_2 bubble rupture during the initiation corrosion. Very high similarity

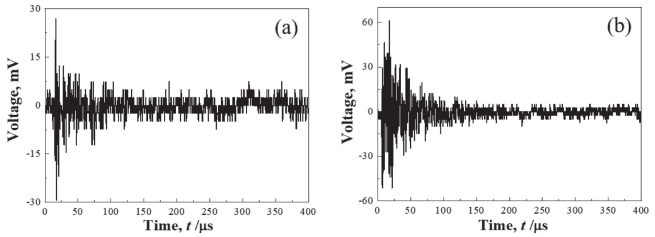

Fig. 5 Typical AE waveforms of H_2 bubble growth during the initial corrosion of AZ31 alloy under the NaCl (a) and Na_2SO_4 (b) solution droplets.

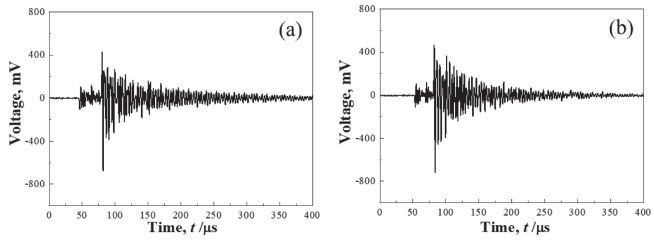

Fig. 6 Typical AE waveforms of H_2 bubble rupture during the initial corrosion of AZ31 alloy under the NaCl (a) and Na_2SO_4 (b) solution droplets.

can be easily found in the waveforms between the two cases. Both waveforms are consisted of two parts, i.e., a front continuous-type part of about 60 μs and the following part of main burst-type peak with the subsequent fading part. According to one of our recent reports,[44] the front part is corresponding to the development of a hole in the liquid film of H_2 bubble; while the following part is associated with the bubble collapse which is concurrent with the growth of the hole and the development of radial wrinkles. Considering the complexity of bubbling phenomenon,[45–47] AE signals indeed provide a unique insight into the rupture dynamics from the acoustical perspective.

Figure 7 shows the cross-plot of amplitude and duration of AE signals during the later corrosion, i.e., filiform corrosion and pitting corrosion under the droplets of NaCl and Na_2SO_4 solution, respectively. It was found that AE parameters of amplitude and duration exhibit a considerable sensitivity to the filiform and pitting corrosion. Suggestively, pitting corrosion tended to produce AE signals with a slightly longer duration than the filiform corrosion signals. The typical AE waveforms of filiform and pitting corrosion were carefully compared, as presented in Fig. 8. Despite not so distinct, some difference between them can be reflected in the AE waveform. The AE signal during filiform corrosion is relatively simple and close to the burst-type waveform with relatively short duration; while the signal during pitting corrosion with slightly long-duration seems to be more close to a resonant waveform of H_2 bubble evolution that was reported in steel corrosion.[23,25,29] According to *in-situ* observations, AE signals during filiform and pitting corrosion

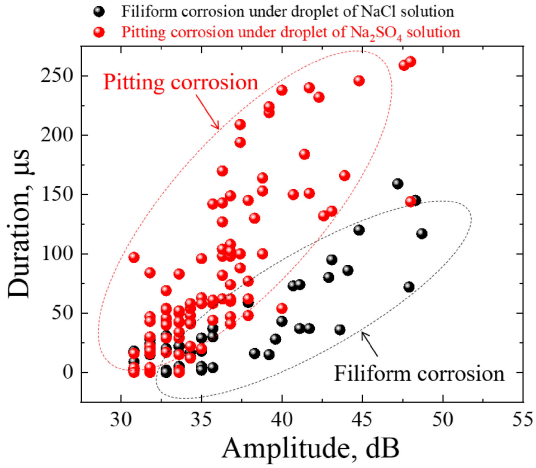

Fig. 7 The cross-plot of amplitude and duration of the AE signals during the filiform corrosion and pitting corrosion of AZ31 alloy under different droplets of NaCl and Na_2SO_4 solution.

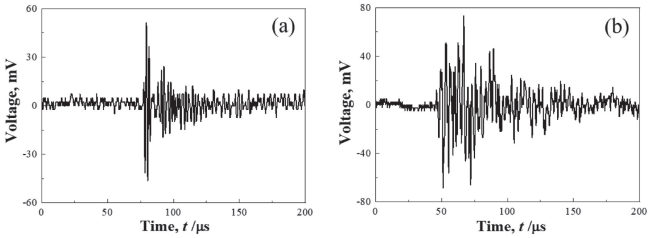

Fig. 8 Typical AE waveforms during the filiform (a) and pitting (b) corrosion of AZ31 alloys under the NaCl and Na_2SO_4 solution droplets.

were correlated with H_2 bubble evolution. A comparison of the typical event of H_2 bubble evolution was shown in Fig. 9. The difference in AE waveforms may be understood based on the different evolution of H_2 bubble in terms of size, shape, and position during the filiform and pitting corrosion. As schematically illustrated in Fig. 9, the bubble at the filament head during filiform corrosion grew in regularly-round shape before rupturing near the metal surface; while the other case of pitting corrosion was always observed with irregularly-shaped bubble growing and rupturing on the corrosion products surface near the pit mouth.

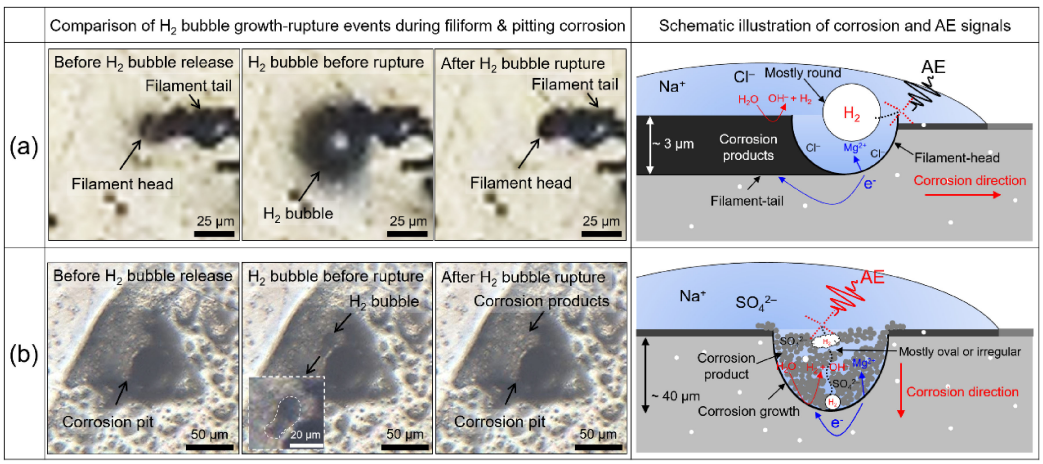

Fig. 9 Comparison and schematic illustration of the typical growth-rupture events of H_2 bubbles and AE signals during filiform corrosion under NaCl solution droplet (a) and pitting corrosion under Na_2SO_4 solution droplet (b).

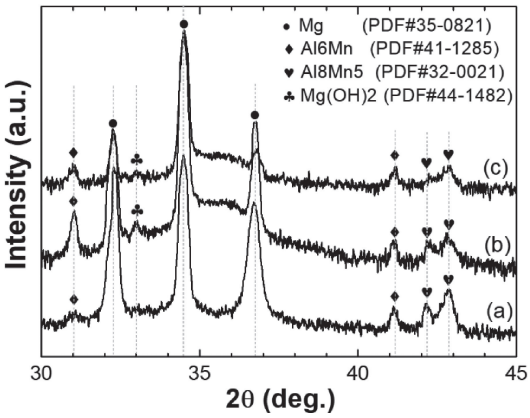

Fig. 10 XRD patterns of AZ31 alloy: (a) Raw surface; (b) After filiform corrosion under NaCl solution droplet; (c) After pitting corrosion under Na_2SO_4 solution droplet.

3.4 Corrosion products and corrosion morphologies

Figure 10 shows the XRD patterns of AZ31 alloy comparing the difference before and after corrosion testing. It is indicated that the main corrosion products of both cases are $Mg(OH)_2$ (brucite). This is in accordance to the previous studies which confirmed the formation of brucite from the atmospheric corrosion of pure Mg and Mg alloys.[48,49] A consensus on the corrosion products has reached regarding the atmospheric corrosion of Mg alloys, i.e., the early stage of Mg corrosion produced brucite and further corrosion will include the role of CO_2 producing magnesium carbonates.[5–8,12,20] This view was confirmed with XRD measurements.[50] The absence of magnesium carbonates in the corrosion products suggesting the corrosion of AZ31 alloy in the present study should be in the early stage of atmospheric corrosion when the role of CO_2 was not involved yet.

Figure 11 shows the morphologies of filiform and pitting corrosion based on post-inspection. Firstly, for the filiform corrosion (Fig. 11(a)), H_2 bubble traces along the filament path were clearly confirmed, which indicates that the filament path periodically passivated and activated during the filiform corrosion.[15] Secondly, as shown in Fig. 11(c), the relative position among the Al-Mn inclusions, corrosion initiation site, and filament path suggested the corrosion evolution in AZ31 alloy might be independent on the role of Al-Mn inclusions. This is consistent with the reports on the ignorable role of Al-Mn inclusions in the initiation and propagation of atmospheric corrosion of AZ31 alloy.[5,6,19] Moreover, the maximum depth of the filament path and the localized corrosion was confirmed to be only few micrometers. The localized corrosion along the filament path, which was reported to be pitting corrosion,[20] seemed to certain areas appearing to shallowly activate and passivate again. Regarding the pitting corrosion presented in Fig. 11(b), it was confirmed that a single pit and some short corrosion filaments were caused. These short corrosion filaments formed at the early stage of initial corrosion with no AE signals were so shallow and indiscernible under the XCT scanning with a 0.8 µm resolution. Therefore, the pitting corrosion with an approx. 41 µm depth dominated the main corrosion behavior under the Na_2SO_4 solution droplet. From the relative position of Al-Mn inclusion and pit, one may draw the similar conclusion that pit initiation was independent of the role of Al-Mn inclusions.[5,6,19] However, the Al-Mn inclusions existing inside the corrosion product might have played some role in the pit growth by considering the cathodic characteristic of Al-Mn inclusion to the Mg

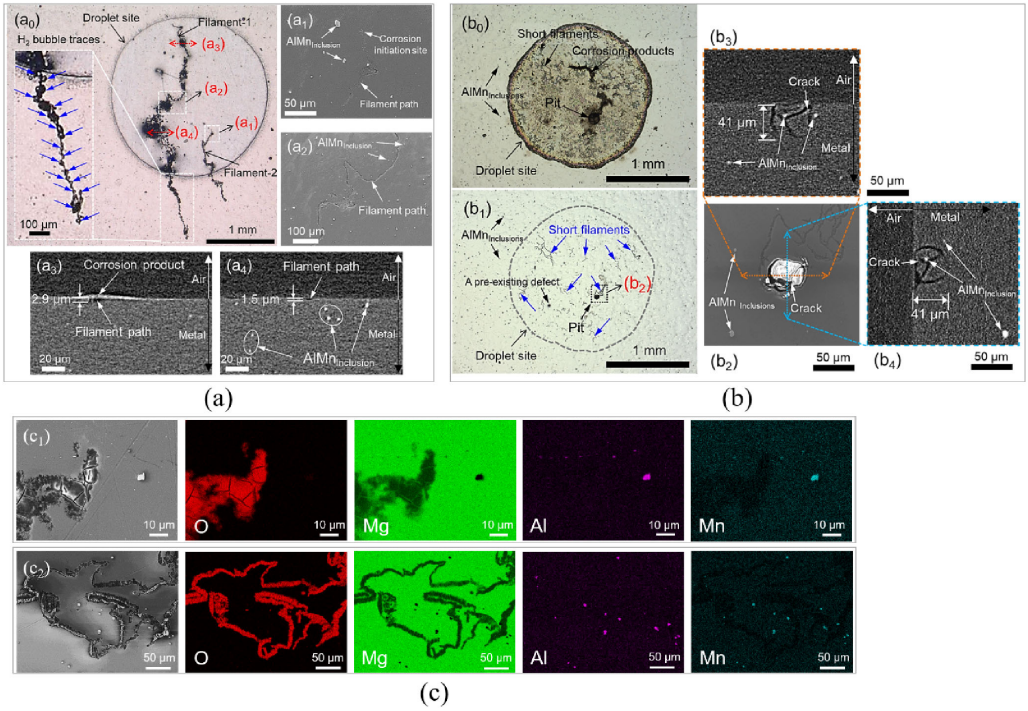

Fig. 11 Corrosion morphologies of AZ31 alloy after corrosion testing: (a) Filiform corrosion from NaCl solution droplet; (b) Localized corrosion under Na_2SO_4 solution droplet; (c) SEM-EDS elemental analysis of Al-Mn inclusions near the filiform corrosion initiation site (c_1) and propagation path (c_2). (a_0), (b_0), (b_1) OM images; (a_1), (a_2), (b_2), (c_1), (c_2) SEM images; (a_3), (a_4), (b_3), (b_4) XCT images.

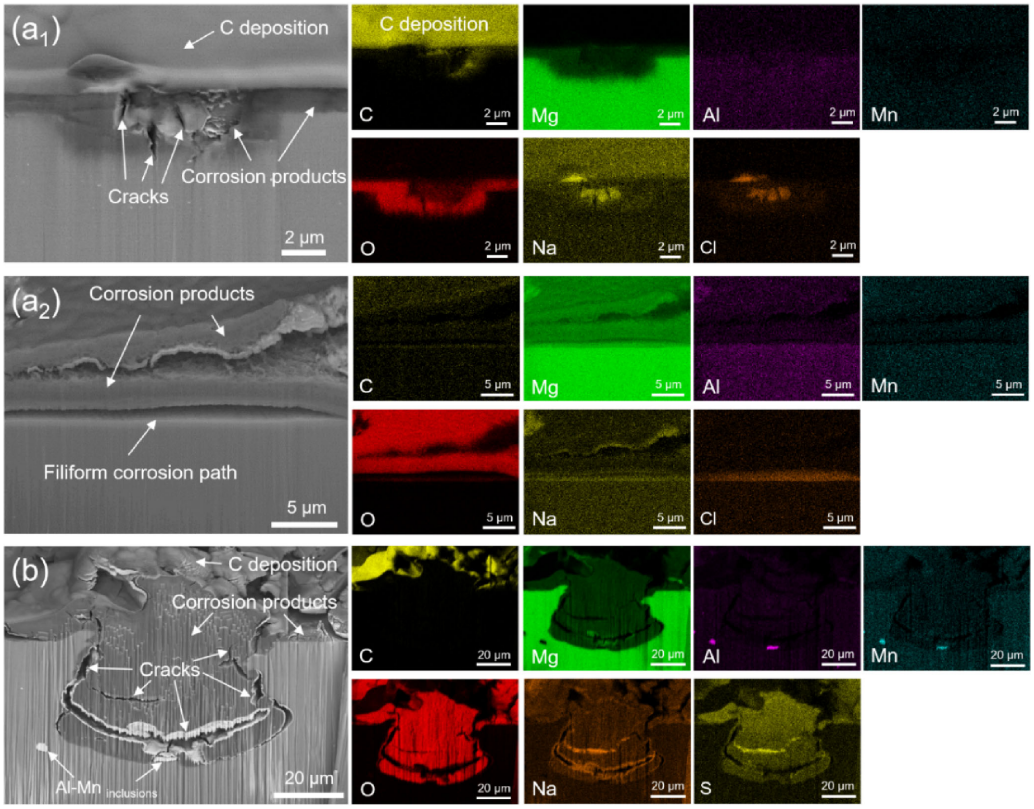

Fig. 12 SEM images and the corresponding EDS elemental mapping of the cross-section of the relevant corrosion sites of AZ31 alloy: (a_1)–(a_2) The typical path of the filiform corrosion developed under NaCl solution droplet; (b) The pit with corrosion products containing cracks developed under Na_2SO_4 solution droplet.

matrix.[9,11] Moreover, some cracks were observed within the corrosion products inside the pit.

Figure 12 shows the FIB-SEM-EDS analysis of the cross-section of filiform corrosion path and corrosion pit. Firstly, it clearly reveals the distinct depth and morphology of filiform corrosion and pitting corrosion. Second, the main aggressive ions of chloride and sulfate was observed to be enriched on the bottom of filiform corrosion path or pit bottom or inside the corrosion products. Moreover, some vertical cracks (parallel to specimen depth direction) and horizontal cracks (parallel to specimen surface) are observed inside the corrosion products of filiform corrosion path and pit, respectively. There cracks should be another important source of AE signals. However, it is still unknown whether these cracks formed during the deposition of corrosion products during the corrosion test or during the drying process after the corrosion test. Therefore, whether they contributed to AE signals during the corrosion process are still questions remained to investigate in the future work.

Figure 13 shows the morphologies of surface films formed during the two corrosion tests. It is observed that the surface film formed in NaCl solution is slightly thicker but more defective with pores and discontinuities through the film; while the film formed in the latter case is relatively thin but appeared to be more compact. On the other hand, chlorine (Cl) is not observed in the surface film formed in NaCl droplet, whereas existence of sulfur (S) in the surface film formed in Na_2SO_4 droplet was confirmed, which are generally consistent with the SEM observation and XPS analysis of the surface films formed on Mg-3Zn alloy after

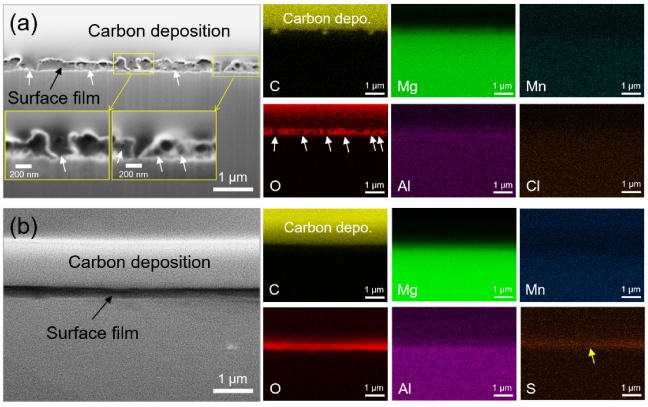

Fig. 13 Cross-sectional SEM images and corresponding EDS maps of two random sites nearby the filiform corrosion (a) and pitting corrosion (b) on AZ31 alloy exposed to the droplets of NaCl and Na_2SO_4 solution, respectively.

immersion in NaCl and Na_2SO_4 solution.[51] The difference in the surface films of two cases should be attributed to the more aggressiveness of chloride ions[52,53] in the NaCl corrosion and the effect of sulfate ions[51] in the film formation process in the latter case.

Figure 14 shows the morphological analysis of filament tail and head of filiform corrosion propagation. From the typical discontinuous morphology of the filament path, it is indicated that the filament front propagated in steps. More importantly, the elemental map reflected a concentration gradient of chlorine (Cl) ions from the filament tail to the

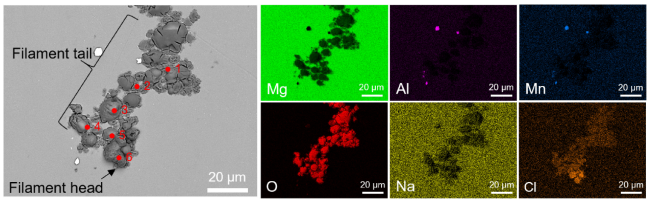

Fig. 14 SEM images and corresponding EDS maps around the filament head of filiform corrosion on AZ31 alloy exposed to the droplet of NaCl solution.

Table 1 EDS analysis of the positions 1–6 (as marked in Fig. 14) along the filiform corrosion propagation of AZ31 alloy (mass%) exposed to NaCl solution droplet.

Relative positions of interest		Cl	O	Mg
	Point 1	0.4	42.2	52.8
	Point 2	5.1	41.3	48.7
Filament tail	Point 3	5.3	42.7	47.2
	Point 4	5.8	44.5	42.5
	Point 5	8.6	42.0	43.8
Near filament head	Point 6	15.5	48.6	22.9

filament head. Further EDS point analysis of points 1–6 as marked in Fig. 14 was given in Table 1. The constituents of these specific spots relative to the filament tail and filament head highlight the enrichment of Cl^- near the filament head. The difference of Cl^- content between filament head region (point 6, 15.5 mass%) and the behind tail (point 1, 0.4 mass%) can be as high as 38 times. The typical stepwise growth of filiform corrosion and concentrated Cl^- at the filament head are consistent with the previous reports on the filiform corrosion in iron[54,55] and Mg alloy[15–20,51–53,56,57] when exposed to NaCl solution.

4. Discussion

In this study, based on *in-situ* surface observations, the corrosion process of AZ31 alloy under different salt solution droplets was divided into two regions, including the initial corrosion and later corrosion stages.

4.1 Initial corrosion stage

Initially, the corrosion was observed to develop in terms of the evolution of single H_2-bubbles at multiple and random sites in two cases. This should be due to the existence of random defects in the $MgO/Mg(OH)_2$ layer of Mg alloy.[3] Once exposed in the liquid solution, the Mg alloy can suffer from localized corrosion attack which was attributed to an electrochemical corrosion process involving anodic Mg dissolution and H_2 evolution[58] through the reactions[59,60] below.

Anodic reaction: $Mg \rightarrow Mg^{2+} + 2e^-$ (1)

H_2 evolution reaction (HER):

$2H_2O + 2e^- \rightarrow 2OH^- + H_2$ (2)

O_2 reduction reaction (ORR):

$O_2 + 2H_2O + 4e^- \rightarrow 4OH^-$ (3)

Overall H_2 bubble release reaction:

$Mg + 2H_2O \rightarrow Mg^{2+} + 2OH^- + H_2\ (g)$ (4)

Corrosion products formation:

$Mg^{2+} + 2OH^- \rightarrow Mg(OH)_2$ (5)

Afterwards, the corrosion products precipitated and covered the localized corrosion sites. The surface became temporarily "quiet" both in surface observations and AE detection.

4.2 Later corrosion stage: Chloride-induced filiform corrosion vs. sulfate-induced pitting corrosion

In the later stage, filiform corrosion propagating horizontally and pitting corrosion growing towards depth direction dominated the main corrosion behavior under NaCl and Na_2SO_4 solution droplet, respectively. The mechanism beneath the distinct corrosion behavior may be understood in terms of different surface film properties and different aggressiveness of Cl^- and SO_4^{2-} ions.

First of all, as shown in Fig. 13, the surface film formed in Na_2SO_4 solution is relatively compact while NaCl solution led to a defective layer with pore-like imperfections through the film. On the other hand, the Cl^- is more aggressive than SO_4^{2-} in attacking the Mg alloys for the smaller diameter and stronger penetrability that enabled an easier enrichment in the mobile anodic head of filament path,[51–53] as evidenced in Fig. 14 and Table 1. For the filiform corrosion under NaCl solution droplet, the stepwise growth of filiform corrosion, as shown in Figs. 3(a), 11(a), and 14, should be controlled with a mechanism involving a cyclic behavior of successive formation of new anodic sites, Mg dissolution, cathodic reaction-induced high pH and enhanced precipitation of corrosion products, anodic deactivation of the corroding surface, and formation of another anodic sites. In details, the filament head acted as the mobile local anode, which is evidenced by the concentrated Cl^- in the filament head (Fig. 14), and the filament tail behind worked as the galvanically coupled cathode region.[15–20,51–53,56,57] Dissolution of Mg through the reaction (1) in a simplified form was accompanied by the cathodic reactions (2)–(3)[60] which would cause the increase of pH. The pH was estimated to increase up as high as 12.5 for pure Mg exposed to NaCl solution by a scanning vibrating electrode technique.[56] The elevated pH would facilitate the precipitation of corrosion products through reducing the solubility of $Mg(OH)_2$.[56,57] The combination of high pH and precipitation of corrosion products would cause anodic activity to switch off and therefore limit the depth of the observed filiform corrosion attack,[55,56] as observed in Figs. 11(a) and 12(a), rather than the deep pit (Fig. 12(b)). Afterwards, due to the volume expansion of corrosion products and H_2 bubble rupturing,[54,55] NaCl solution leaked from the previous corrosion solution pool and the new region was exposed as the filament head, while the previous anode site transformed to a cathode site with the forward progress of advancing filament front. This could be evidenced by the periodic release of H_2 bubbles around the filament head and the stepwise growth traces, as observed in Figs. 3(a), 9(a), 11(a), and 14. In contrast, for the pitting corrosion under Na_2SO_4 solution droplet, SO_4^{2-} ions of weak penetrating ability and mild aggressiveness

were difficult to migrate in the relatively compact surface film.[51–53] On the other hand, the H_2 bubble evolution, as observed in Figs. 3(b) and 9(b), was also relatively moderate and could not facilitate the spreading of corrosion solution to cause another new anodic site in the neighboring region. Instead, SO_4^{2-} ions tend to locally attack the weak site of surface film and cause a pit, and then enrich at the bottom of pit to accelerate the Mg dissolution in the vertical direction.[51] Regarding the temporary passivation of pit growth, it may be understood by the partially protective corrosion product layer. As the corrosion proceeded and the corrosion products accumulated inside the pit, the corrosion can be stopped when the pit bottom/dissolution interface was covered by corrosion products. However, the main corrosion products formed as brucite of porous structure which can be penetrated again by the sulfate ions.[52,53,58,59] This may account for the temporary passivation of pitting corrosion during 5.9–9.4 h and 12.5–14.4 h, as presented in Fig. 4(b).

4.3 AE monitoring of filiform corrosion and pitting corrosion

In this work, it is interesting to find that AE parameters of amplitude and duration are able to reflect the difference of filiform and pitting corrosion of AZ31 alloy in relation to different salt droplet corrosion attack. Although there was some signal overlapping on their cross plot (Fig. 7), it suggests that the pitting corrosion under Na_2SO_4 solution droplet tended to produce AE signals of slightly long-duration; while AE signals of filiform corrosion were with relatively short-duration (Figs. 7 and 8). Amplitude and duration has been adopted to identify different pitting steps[25] and estimate the pit morphology[29] in investigating pitting corrosion in steels. Especially, according to a specific report,[29] long-duration AE signals were correlated with an occluded morphology of pit and relatively short-duration AE signals were associated with an open morphology of pit. From this point, the pitting corrosion of AZ31 alloy under Na_2SO_4 droplet could be regarded as an occluded morphology, as presented in Fig. 12, because the deposited corrosion products in the pit acted like a thick pit cover; while the filiform corrosion under NaCl droplet might be seen as the result of a series of open-morphological, shallow pitting, as revealed in Figs. 9, 11, 12, and 14, because the concurrent H_2 bubbles ruptured at the filament head near the metal surface.

By carefully comparing with *in-situ* observations, the evolution of H_2 bubbles during filiform and pitting corrosion were considered to be the main source for the detected AE signals. The AE difference between the two cases might be tentatively understood as follows. Firstly, the acoustic feature in terms of frequency of a growing bubble has been correlated with the bubble size.[43] The distinct morphology, shape, and size of the H_2 bubble evolution, as highlighted in Fig. 9, may partially explain the AE difference between the two cases. Another point is probably correlated with the position of the rupture event of H_2 bubbles. The bubbles during filiform corrosion mostly formed nearby the filament head and finally ruptured on the metal surface. However, bubbles during pitting corrosion were likely to be formed at the pit bottom first and ruptured at the pit mouth after they moved upward. Therefore, the bubbles during pitting corrosion mostly ruptured on the surface of accumulated corrosion products (Fig. 9). Occurrence site of bubbling at different solid surface (metal vs. oxide/hydroxides) may greatly affect the propagation and attenuation of AE signals, during which the waveform and frequency probably changed.[60] Moreover, it must be quoted that the friction phenomenon of the evolving H_2 bubbles inside the pit or on the corrosion products, as proposed by Fregonese *et al.*,[23] might also have contributed to the difference in AE behaviors.

This qualitative explanation above may provide some clues to understand the difference of corrosion behavior and the concurrent AE signals of AZ31 alloy exposed to different salt droplets. However, a direct visualization of AE signals from breakdown of the surface films and the cracking inside the corrosion products requires future works on how to separately control and quantitatively test the specific process. Despite the existing uncertainties, the present work has demonstrated that AE signals in terms of specific parameters, such as amplitude and duration, are sensitive to the corrosion mode of Mg alloys in relation to the H_2 bubble evolution under salt droplets of different corrosion media. Especially, AE is a non-invasive, physical NDE technique and its operation is rarely affected by the changing atmospheric environment and specimen conditions. Therefore, AE-based NDE method, especially inspired by the findings of this work, should be with great potential as a complementary monitoring approach with other sensors or probes techniques that are based on electrochemical measurements.[61] Furthermore, the high sensitivity of the AE signal to the growth and rupture of H_2 microbubbles shown in this work should open a new path for understanding the complex phenomenon with bubbling based on AE method.

5. Conclusions

This study proposed AE monitoring with *in-situ* observations to comparatively investigate the corrosion behavior of AZ31 alloy exposed to droplets of NaCl and Na_2SO_4 solution, respectively. Some conclusions are drawn below.

(1) After a short initial corrosion accompanied by the growth and rupture of single H_2 bubbles, the later corrosion behavior of AZ31 alloy was observed to mainly develop into filiform corrosion under NaCl solution droplet and pitting corrosion under Na_2SO_4 solution droplet, which were concurrent with H_2 bubble evolution at the filament head and pit mouth, respectively. Enrichment of chloride and sulfate ions were observed to be at the filament head and pit bottom, respectively.

(2) AE signals were detected in both cases. Amplitude and duration of AE parameters were found to well identify filiform corrosion and pitting corrosion of AZ31 alloy under NaCl and Na_2SO_4 solution droplets.

(3) AE signals were mainly correlated with the observed evolution of H_2 bubbles of different shapes and positions, i.e., regularly round bubbles grew and ruptured near the filament head at the metal surface during filiform corrosion; whereas irregularly-shaped

bubbles grew and ruptured at the pit mouth during pitting corrosion. However, breakdown of the oxide surface film that is difficult to observe, as well as the post-observed cracks within the corrosion products of filiform corrosion and pitting corrosion cannot be excluded from the possible sources of AE signals.

Acknowledgements

This work was supported by JSPS KAKENHI Grant Number JP21K14435.

REFERENCES

1) U.M. Chaudry, S. Tekumalla, M. Gupta, T.S. Jun and K. Hamad: Crit. Rev. Solid State Mater. Sci. **47** (2022) 194–281.
2) H. Liu, F. Cao, G.L. Song, D. Zheng, Z. Shi, M.S. Dargusch and A. Atrens: J. Mater. Sci. Technol. **35** (2019) 2003–2016.
3) M. Esmaily, J.E. Svensson, S. Fajardo, N. Birbilis, G.S. Frankel, S. Virtanen, R. Arrabal, S. Thomas and L.G. Johansson: Prog. Mater. Sci. **89** (2017) 92–193.
4) G.E. Totten, L. Xie and K. Funatani (ed.): *Handbook of Mechanical Alloy Design*, (Marcel Dekker, Inc., New York, 2004) pp. 487–538.
5) J. Liao, M. Hotta, S. Motoda and T. Shinohara: Corros. Sci. **71** (2013) 53–61.
6) J. Liao and M. Hotta: Corros. Sci. **112** (2016) 276–288.
7) M. Jönsson, D. Persson and C. Leygraf: Corros. Sci. **50** (2008) 1406–1413.
8) Z. Cui, X. Li, K. Xiao and C. Dong: Corros. Sci. **76** (2013) 243–256.
9) M.C. Merino, A. Pardo, R. Arrabal, S. Merino, P. Casajús and M. Mohedano: Corros. Sci. **52** (2010) 1696–1704.
10) R. Arrabal, B. Mingo, A. Pardo, E. Matykina, M. Mohedano, M.C. Merino, A. Rivas and A. Maroto: Corros. Sci. **97** (2015) 38–48.
11) R. Arrabal, A. Pardo, M.C. Merino, S. Merino, M. Mohedano and P. Casajús: Mater. Corros. **62** (2011) 326–334.
12) M. Jönsson, D. Persson and D. Thierry: Corros. Sci. **49** (2007) 1540–1558.
13) M. Strebl and S. Virtanen: J. Electrochem. Soc. **166** (2019) C3001–C3009.
14) W. Liu, F. Cao, A. Chen, L. Chang, J. Zhang and C. Cao: Corros. Sci. **52** (2010) 627–638.
15) O. Lunder, J.E. Lein, S.M. Hesjevik, T.K. Aune and K. Nişancioğlu: Mater. Corros. **45** (1994) 331–340.
16) Z. Shao, M. Nishimoto, I. Muto and Y. Sugawara: Corros. Sci. **192** (2021) 109834.
17) E. Kakutani, K. Fujio, M. Jotoku, A. Yamamoto and H. Tsubakino: J. Jpn. Inst. MET. **72** (2008) 420–426.
18) N. Hara, Y. Kobayashi, D. Kagaya and N. Akao: Corros. Sci. **49** (2007) 166–175.
19) X. Yan, L. Chen, X. Xu, Y. Zhao and M. Zhao: Adv. Eng. Mater. **23** (2021) 2100396.
20) Y. Wang, C. Zhen, Z. Zhang and Z. Tao: PLoS One **15** (2020) e0234981.
21) J. Wright and A. Colling: *Seawater: Its Composition, Properties and Behaviour*, 2nd ed., (Pergamon, 1995).
22) C.B. Scruby: J. Phys. E **20** (1987) 946–953.
23) M. Fregonese, H. Idrissi, H. Mazille, L. Renaud and Y. Cetre: Corros. Sci. **43** (2001) 627–641.
24) C. Jirarungsatian and A. Prateepasen: Corros. Sci. **52** (2010) 187–197.
25) J. Xu, X.Q. Wu and E.H. Han: Corros. Sci. **53** (2011) 1537–1546.
26) K. Wu, W.S. Jung and J.W. Byeon: Mater. Trans. **56** (2015) 398–403.
27) K. Wu, W.S. Jung and J.W. Byeon: Mater. Trans. **56** (2015) 587–592.
28) K. Wu, W.S. Jung and J.W. Byeon: Corros. Sci. **105** (2016) 8–16.
29) K. Wu and J.W. Byeon: Corros. Sci. **148** (2019) 331–337.
30) K. Wu and J.Y. Kim: Corros. Sci. **180** (2021) 109224.
31) Y. Wu, J. Nong, S. Yuan, Q. Guo and J. Xu: Corros. Sci. **183** (2021) 109308.
32) K. Wu, K. Ito, I. Shinozaki, P. Chivavibul and M. Enoki: Materials **12** (2019) 2569.
33) K. Wu, F. Briffod, K. Ito, I. Shinozaki, P. Chivavibul and M. Enoki: Mater. Trans. **60** (2019) 2151–2159.
34) D.G. Chakrapani and E.N. Pugh: Metall. Trans. A **6** (1975) 1155–1163.
35) H.M. Zhou, J.Q. Wang, Q.S. Zang and E.H. Han: Key Eng. Mater. **353–358** (2007) 327–330.
36) J. Orlikowski and K. Darowicki: Electrochim. Acta **56** (2011) 7880–7884.
37) M. Knapek, P. Minárik, J. Čapek, R. Král, J. Kubásek and F. Chmelík: Corros. Sci. **145** (2018) 10–15.
38) H.Y. Kim, J.Y. Kim, S.M. Lee and J.W. Byeon: Mater. Trans. **58** (2017) 123–126.
39) Z. Zhang, Z. Zhao, P. Bai, X. Li, B. Liu, J. Tan and X. Wu: J. Alloy. Compd. **878** (2021) 160334.
40) K. Ito and M. Enoki: Mater. Trans. **48** (2007) 1221–1226.
41) Chapter 3 AE parameters, in: Y. Mizutani (ed.): *Acoustic Emission Testing*, (The Japanese Society for Non-Destructive Inspection (JSNDI), 2008) pp. 30–35.
42) K. Wu, N. Yatagai, T. Shiraiwa and M. Enoki: EUROCORR2023, Aug. 29, (2023).
43) M. Minnaert: Philos. Mag. **16** (1933) 235–248.
44) K. Wu, N. Yatagai, T. Shiraiwa and M. Enoki: Proc. of JSNDI Fall Conf. 2023, Oct. 5–6, (2023) pp. 227–228.
45) T. Takata, M. Enoki, P. Chivavibul, A. Matsui and Y. Kobayashi: Mater. Trans. **57** (2016) 674–680.
46) S.H. Baek, K. Wu, H.S. Shim, D.H. Lee, J.G. Kim and D.H. Hur: Meas. **109** (2017) 18–26.
47) A.T. Oratis, J.W.M. Bush, H.A. Stone and J.C. Bird: Science **369** (2020) 685–688.
48) R. Lindstrom, L.G. Johansson, G.E. Thompson and J.E. Svensson: Corros. Sci. **46** (2004) 1141–1158.
49) M. Shahabi-Navid, Y. Cao, J.E. Svensson, A. Allanore, N. Birbilis, L.G. Johansson and M. Esmaily: Sci. Rep. **10** (2020) 20972.
50) K. Wu and M. Enoki: Virtual EUROCORR2021, Sep. 22, (2021).
51) H. Wang, Y. Song, D. Shan and E.-H. Han: Corros. Commun. **2** (2021) 24–32.
52) M.G. Acharya and A.N. Shetty: J. Magnes. Alloy. **7** (2019) 98–112.
53) L. Wang, T. Shinohara and B.P. Zhang: J. Alloy. Compd. **496** (2010) 500–507.
54) S.X. Li and L.H. Hihara: Corros. Eng. Sci. Technol. **45** (2010) 49–56.
55) J. Weissenrieder and C. Leygraf: J. Electrochem. Soc. **151** (2004) B165–B171.
56) G. Williams and H.N. McMurray: J. Electrochem. Soc. **155** (2008) C340–C349.
57) G. Williams, H.L. Dafydd and R. Grace: Electrochim. Acta **109** (2013) 489–501.
58) G. Song and A. Atrens: Adv. Eng. Mater. **1** (1999) 11–33.
59) M. Strebl, M. Bruns and S. Virtanen: J. Electrochem. Soc. **167** (2020) 021510.
60) J. Cuadra, P. Vanniamparambil, D. Servansky, I. Bartoli and A. Kontsos: J. Sound Vib. **341** (2015) 222–236.
61) D.-H. Xia, C.-M. Deng, D. Macdonald, S. Jamali, D. Mills, J.-L. Luo, M.G. Strebl, M. Amiri, W. Jin, S. Song and W. Hu: J. Mater. Sci. Technol. **112** (2022) 151–183.